



# Interfacial engineering to achieve an energy density of over 200 Wh kg<sup>-1</sup> in sodium batteries

Yuqi Li<sup>1,2</sup>, Quan Zhou<sup>1,3</sup>, Suting Weng<sup>1</sup>, Feixiang Ding<sup>1,4</sup>, Xingguo Qi<sup>1,3</sup>, Jiaze Lu<sup>1</sup>, Yu Li<sup>1,2,4</sup>,  
Xiao Zhang<sup>1,2</sup>, Xiaohui Rong<sup>1,5</sup>, Yaxiang Lu<sup>1,3,5</sup>✉, Xuefeng Wang<sup>1,6</sup>, Ruijuan Xiao<sup>1,5</sup>,  
Hong Li<sup>1,2,4,5,6</sup>, Xuejie Huang<sup>1</sup>, Liquan Chen<sup>1</sup> and Yong-Sheng Hu<sup>1,2,3,4,5</sup>✉

**Sodium-based batteries have attracted wide interests in the academic and industrial fields. However, their energy density is still lower than that of Li-based batteries. Here we report an initial anode-free Na battery with an energy density of over 200 Wh kg<sup>-1</sup>, which is even higher than that of the commercial LiFePO<sub>4</sub>/graphite battery. Through introducing graphitic carbon coating on the Al current collector and boron-containing electrolytes in the battery, we show that uniform nucleation and robust interphases enable reversible and crack-free Na deposition. Benefiting from the synergetic effects derived from the built cooperative interfaces, the cycling lifetime of the Na battery without applying additional pressure reaches 260 cycles, which is the longest life for large-size cells with zero excess Na. The insights gained from the Na plating/stripping behaviour and interfacial chemistry in this work pave the way for further development of Na batteries with even higher performance.**

Considering the abundant Na reserve and its worldwide distribution, the Na-ion battery (NIB) is a cost effective choice for electrical energy storage, particularly, in large-scale grid decarbonization<sup>1</sup>. However, limited by the relatively large atomic size and weight of Na, the energy density of current NIBs is generally below 160 Wh kg<sup>-1</sup>, which is lower than that of commercial Li counterparts<sup>2</sup>. A promising solution towards higher energy is replacing the insertion-type electrodes in NIBs such as carbons with ultra-thin Na metal (1,166 mAhg<sup>-1</sup> and -2.71 V versus standard hydrogen electrode potential) to fabricate Na metal batteries (NMBs)<sup>3,4</sup>. Nevertheless, due to the soft and sticky properties of metallic Na, processing and moulding are too difficult to produce the ultra-thin Na metal anode. On the other hand, NMBs with thick anodes that contain excess amounts of Na may sacrifice energy density. In addition, the poor air stability of Na metal (even in dry room conditions) is very unfavourable for large-scale manufacture of NMBs<sup>5</sup>.

The anode-free Na battery (AFNB) configuration may offer a solution to the above problems<sup>6,7</sup>. In AFNB, the ‘real anode’ is electrochemically in situ formed during the first charging process; the Na formed at the anode side is always encapsulated without air exposure, and no Na is wasted as active Na<sup>+</sup> shuttles are completely from cathode materials. This not only facilitates the manufacturing process but also boosts the energy density of AFNBs. However, during the AFNB operation, active Na is consumed<sup>8,9</sup> and easy breakage and reconstruction of the solid electrolyte interphase (SEI) is induced by the large volume change of the deposited Na metal and the high solubility of SEI components (such as Na alkyl carbonates)<sup>10,11</sup>. These lead to rapid capacity decay. The uneven deposition morphology also induces ‘dead Na’ during the repeated plating and stripping, resulting in a low Coulombic efficiency (CE). Thus, both opportunities and challenges exist in the AFNBs. However, unlike anode-free Li batteries, AFNBs have received less attention<sup>12–15</sup>.

To achieve high-performance AFNBs, it is vital to carefully consider all essential components (including current collectors, electrolytes and cathodes) and their compatibility at the cell level. For current collectors, various substrates such as Cu, Al, Ag, C and so on and their hybrids have been used for Na deposition<sup>8,9,16–19</sup>. Among them, the Al–C hybrid could be an ideal current collector. This is because Al could be used at both the cathode and anode sides, and Al is light and inexpensive. On the other hand, low-cost carbon materials with diverse structures and versatile properties may be a good substrate with sodiophilicity.

Concerning electrolyte selection, 1 M NaPF<sub>6</sub> in diglyme (denoted as PG) has been shown to enable a high average CE of 99.9% in Na–Cu batteries<sup>20</sup>. Among ether-based solvents, diglyme has relatively low viscosity and volatility<sup>21,22</sup>. NaPF<sub>6</sub> can effectively stabilize Na metal as it facilitates the formation of favourable solvation structures for ion transport and the formation of low-impedance SEI<sup>20,23,24</sup>. Therefore, NaPF<sub>6</sub> in diglyme could be a suitable electrolyte formula for AFNBs. However, the depletion of limited Na content during the repeated formation of SEI often takes place in AFNBs; the poor compatibility between electrolytes and cathodes usually results in a relatively low CE in AFNBs. Moreover, the lean state of the electrolytes would accelerate the above failure process.

Prussian blue analogues and V-containing phosphates are common cathode materials for Na batteries, but intrinsic challenges exist<sup>16–19,25</sup>. For example, the interstitial water in Prussian blue analogues is detrimental to cell performance but is difficult to remove; V-based phosphates contain toxic elements. Layered transition metal oxides have been tipped to be promising for high electrochemical performance and facile large-scale fabrication<sup>26</sup>. However, they have been rarely studied for AFNBs, mainly due to the challenge of the transition metal dissolution during cycling. Another issue concerns the mass loading of active cathode materials; in most

<sup>1</sup>Key Laboratory for Renewable Energy, Beijing Key Laboratory for New Energy Materials and Devices, Laboratory for Advanced Materials & Electron Microscopy, Beijing National Laboratory for Condensed Matter Physics, Institute of Physics, Chinese Academy of Sciences, Beijing, China. <sup>2</sup>College of Materials Science and Optoelectronic Technology, University of Chinese Academy of Sciences, Beijing, China. <sup>3</sup>HiNa Battery Technology Co., Ltd., Beijing, China. <sup>4</sup>Huairou Division, Institute of Physics, Chinese Academy of Sciences, Beijing, China. <sup>5</sup>Yangtze River Delta Physics Research Center, Liyang, China. <sup>6</sup>Tianmu Lake Institute of Advanced Energy Storage Technologies, Liyang, China. ✉e-mail: [yxlu@iphy.ac.cn](mailto:yxlu@iphy.ac.cn); [yshu@iphy.ac.cn](mailto:yshu@iphy.ac.cn)

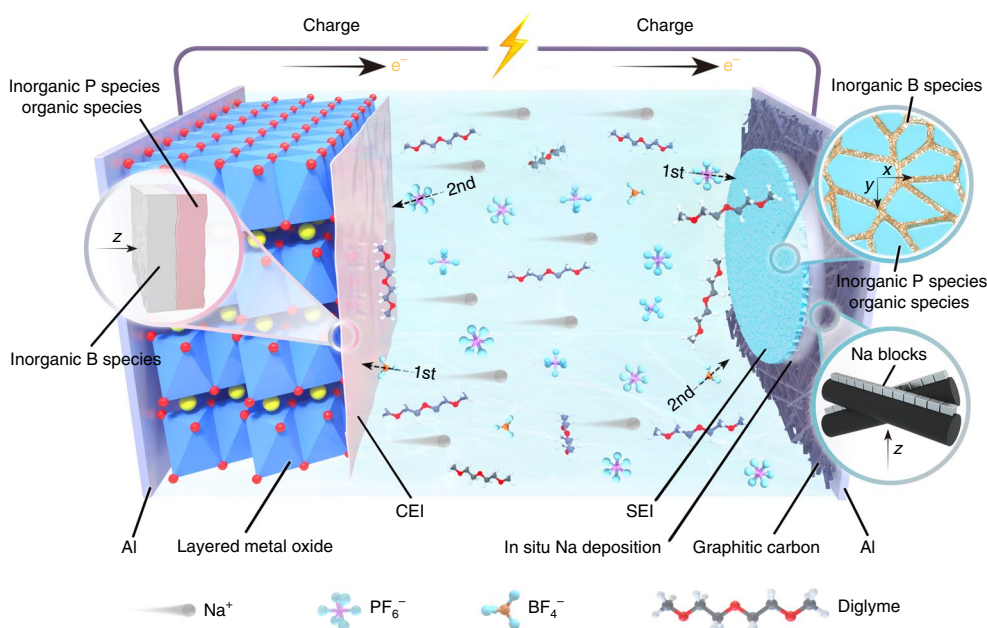


**Fig. 1 | Sodium batteries with cooperative interfaces using a graphitic carbon coating as the current collector and BPG as the electrolyte.** The CEI at the cathode side is induced by the decomposition of the electrolyte in the following sequence:  $\text{NaBF}_4$  decomposes before  $\text{NaPF}_6$  does. The two sequential processes are denoted as ‘1st’ and ‘2nd’ with arrows that are superimposed on the respective salt molecule. Decomposition also takes place at the anode side but with a different sequence;  $\text{NaPF}_6$  decomposes before  $\text{NaBF}_4$  does. These decomposition processes have direct influences on the morphologies of the CEI and SEI. As shown in the inset for the CEI (a vertical view is displayed), a three-dimensional distribution of inorganic B species appears in the inner layer of the CEI whereas inorganic P species and organic species distribution appears in the outer layer. In the outer layer of the SEI (the inset in a planar view), B species shows a two-dimensional distribution (the inner layer is not shown here); a vertical view denotes a sodiophilic graphitic carbon coating enables uniform nucleation of small Na blocks. The shape and thickness of the CEI and SEI are arbitrarily drawn, and the circular SEI is also used to denote the uncompleted Na plating.

reports of Na batteries, the loadings are relatively low, indicating a small amount of Na deposition with little practical significance. In addition, it is challenging to realize large-scale cells, especially when working under practical conditions such as limited electrolytes.

In this study, we adapt a battery setting in which a graphitic carbon-coated current collector is used with no Na content at the anode before the first charging, as shown in Fig. 1. Because carbon contributes a negligible amount of capacity, we term the battery ‘initial anode-free Na batteries’. We use a layered oxide-based  $\text{Na}[\text{Cu}_{1/9}\text{Ni}_{2/9}\text{Fe}_{1/3}\text{Mn}_{1/3}]\text{O}_2$  with a high mass loading of  $>15 \text{ mg cm}^{-2}$ . Instead of the common PG electrolyte formula, we design an electrolyte consisting of  $0.9 \text{ M NaPF}_6$  and  $0.1 \text{ M NaBF}_4$  in diglyme (denoted as BPG). We show that B-containing species (the decomposition products of  $\text{NaBF}_4$ ) play significant roles in both the SEI and cathode electrolyte interphase (CEI). We reveal from combinatorial in situ and ex situ characterization analyses and theoretical simulations that the interfaces formed between different cell components significantly affect the reversible Na plating/stripping. We also demonstrate large-scale Ah-level cells with a high energy density of  $205 \text{ Wh kg}^{-1}$  that are highly reversible, dendrite-free and even crack-free for Na deposition. A long lifetime of 260 cycles is achieved with the use of lean electrolytes ( $2 \text{ g Ah}^{-1}$ ).

### Controlling Na nucleation on current collectors

The initial Na nucleation on the current collector plays a key role in Na deposition. Considering that bare Al foil has been confirmed to be unfavourable for Na nucleation<sup>7,27</sup>, two kinds of current collectors based on Al foil with amorphous and graphitic carbon coating, denoted as AC and GC, respectively, were prepared as investigation models.

Scanning electron microscopy (SEM) images (Fig. 2a,b) about their surface morphology show that the structural unit of AC is a

spotted carbon particle with a size distribution from 60 nm to 150 nm while that of GC is a crossed carbon rod with a diameter distribution from 90 nm to 140 nm. The porosity of GC is obviously larger than that of AC. High-resolution transmission electron microscopy (TEM) images demonstrate that AC presents a disordered microstructure with turbostratic nanodomains (Fig. 2c) while GC displays regular lattice fringes with interlayer spacing of  $\sim 0.33 \text{ nm}$  (Fig. 2d). Raman spectra analyses further confirm the higher ordering associated with fewer defects of GC than that of AC (Supplementary Fig. 1). The high graphitization degree of GC benefits the higher electronic conductivity of GC than that of AC via a four-probe method (Supplementary Fig. 2). Besides, rich pores of GC endow a perfect wetting by the electrolyte (Supplementary Fig. 3).

The  $\text{Na}||\text{AC}$  and  $\text{Na}||\text{GC}$  cells (Supplementary Fig. 4) were first prepared to assess the electrochemical performance ( $>0 \text{ V}$ ) of GC and AC under the PG electrolyte. It can be seen that AC shows a sloping feature with high initial capacity loss (such as adsorption behaviour in disordered carbon at low pyrolysis temperature), whereas GC shows both sloping and plateau regions with low initial capacity loss (such as co-intercalation behaviour in graphite with ether electrolytes)<sup>28</sup>. Further overdischarging the cells below  $0 \text{ V}$  demonstrates the nucleation overpotential of GC ( $16.4 \text{ mV}$ ) is smaller than that of AC ( $25.7 \text{ mV}$ ) (Supplementary Fig. 5), indicating a favourable Na growth on the sodiophilic-ordered carbon surface<sup>29</sup>.

The Na deposition morphology (areal capacity of metallic sodium is  $\sim 2 \text{ mAh cm}^{-2}$ ) in AFNBs ( $\text{AC}||\text{Na}[\text{Cu}_{1/9}\text{Ni}_{2/9}\text{Fe}_{1/3}\text{Mn}_{1/3}]\text{O}_2$  and  $\text{GC}||\text{Na}[\text{Cu}_{1/9}\text{Ni}_{2/9}\text{Fe}_{1/3}\text{Mn}_{1/3}]\text{O}_2$  between  $0 \text{ V}$  and  $4 \text{ V}$  at a current rate of  $0.5 \text{ C}$  ( $1 \text{ C} = 127 \text{ mAh g}^{-1}$ ) using the PG electrolyte was investigated via SEM. The irregular and cracked Na lumps with size distribution from 100 nm to 600 nm are observed on AC (Fig. 2e), while the relatively uniform and small Na pieces with size distribution from 100 nm to 200 nm are formed on GC

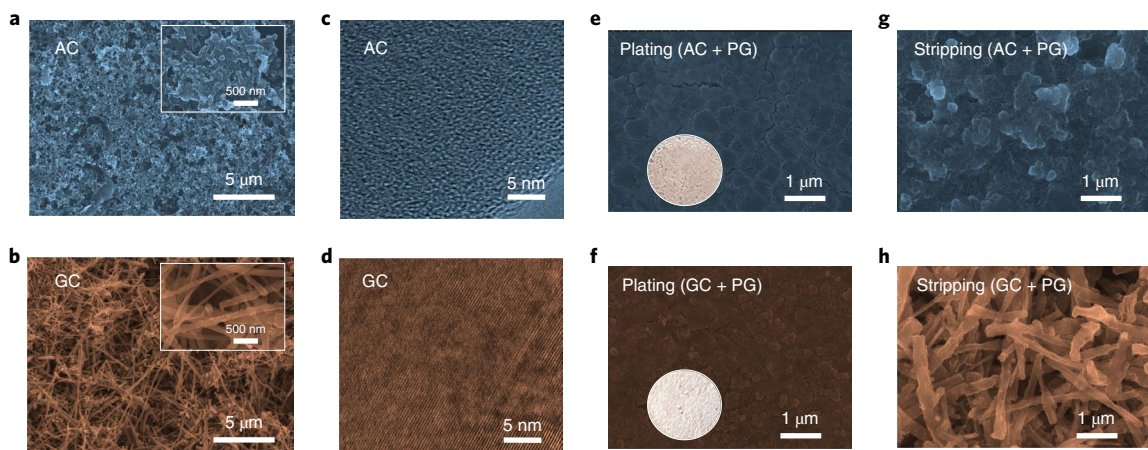


**Fig. 2 | Current collectors and morphologies of Na plating and stripping.** **a,b**, SEM images of AC (**a**) and GC (**b**). The insets show the enlarged SEM images. **c,d**, TEM image of AC (**c**) and GC (**d**). **e,f**, SEM images of Na deposition in the AFNBs using PG plus AC (**e**) and GC (**f**) after ten cycles. The insets show the digital images of Na deposition. **g,h**, SEM images of Na stripping in the AFNBs using PG plus AC (**g**) and GC (**h**) after ten cycles.

(Fig. 2f). The different microscopical textures further affect the macroscopical features shown in the left bottom insets, where the deposited Na on GC shines more and is more compact than that on AC. Further stripping tests reveal that a thick coverage disturbs the intrinsic morphology of AC (Fig. 2g), suggesting a copious SEI or dead Na formation. On the contrary, there is almost no change of GC with a clear rod structure, indicating a thin SEI and less dead Na formation (Fig. 2h). Thus it can be concluded that Na deposition and stripping is better on GC, owing to the favourable nucleation (high uniformity), porous structure (large specific surface area contributes to a low actual current density) and good electron transportation (high reaction reversibility with less dead Na) of GC. The bottom-up Na deposition is strongly affected by the current collector, where the uniform and small Na blocks can reduce the cracks to form a smooth Na layer, as depicted in Fig. 1 and Supplementary Fig. 6.

### Building robust SEI and CEI interfaces

Note that even when GC was employed, few cracks still appeared on the surface of the deposited Na. This means that electrolytes must be designed to enable the formation of both robust SEI and CEI so that the crack formation during long cycling can be prevented from Na deposition. NaBF<sub>4</sub> has been reported to be a potential electrolyte component;<sup>17,30,31</sup> however, due to its limited solubility, we therefore envisage that it can be utilized as an additive. In this study, we use BPG to replace the PG used in the above experiments.

We found that while both PG and BPG show a stable electrochemical window up to 4.5 V versus Na<sup>+</sup>/Na in the linear sweep voltammetry (LSV) curves, BPG has a slightly higher oxidation stability than that of PG (Supplementary Fig. 7). Moreover, BPG has a better wettability on the separator than PG (Supplementary Fig. 8). The Tafel plot of BPG shows a higher exchange current than that of PG (0.087 mA cm<sup>-2</sup> versus 0.038 mA cm<sup>-2</sup>) based on the extrapolation procedure (Supplementary Fig. 9), indicating the introduction of NaBF<sub>4</sub> can facilitate the charge transfer. The Na||Na symmetric cells with BPG also show a lower voltage polarization than that with PG (Supplementary Fig. 10). More importantly, the Na deposition in real AFNBs with GC and BPG presents a very smooth and compact morphology in Fig. 3a. The small Na blocks look to be spliced together and there is no crack on the surface. Replacing GC with AC, the interface healing phenomenon can still be observed with the addition of NaBF<sub>4</sub> (Supplementary Fig. 11), implying NaBF<sub>4</sub> plays a key role in the electrode/electrolyte interface.

To interpret the role of NaBF<sub>4</sub> in building the SEI/CEI layers, the frontier molecular orbital energies (Fig. 3b), including lowest unoccupied molecular orbital (LUMO) energies and highest occupied molecular orbital (HOMO) energies, were calculated to clarify the thermodynamic potential of NaBF<sub>4</sub> in the electrolyte. It can be seen that both LUMO and HOMO energy levels of NaBF<sub>4</sub> are higher than those of NaPF<sub>6</sub>, indicating NaBF<sub>4</sub> will be subsequently reduced on the anode (SEI) but preferentially oxidized on the cathode (CEI) compared with NaPF<sub>6</sub>. More specifically, NaPF<sub>6</sub> decomposes before NaBF<sub>4</sub> at the anode side while NaBF<sub>4</sub> decomposes before NaPF<sub>6</sub> at the cathode side to mainly form inorganic species in interphases, where the two sequential processes are denoted as ‘1st’ and ‘2nd’, as shown in Fig. 1. Diglyme has the highest LUMO and HOMO energy level, which means it is difficult to be reduced but can be easily oxidized to mainly form organic species in interphases. Molecular dynamics (MD) simulations were conducted to analyse the change of solvation structures after the addition of NaBF<sub>4</sub>. In Supplementary Figs. 12 and 13, MD simulation snapshots and typical coordination structures of PG and BPG show that the PG or BPG electrolyte contains many free diglyme molecules and PF<sub>6</sub><sup>-</sup>/BF<sub>4</sub><sup>-</sup> anions considering the high solvent-to-salt ratio of ~7 (ref. <sup>32</sup>). Both PF<sub>6</sub><sup>-</sup> and BF<sub>4</sub><sup>-</sup> can enter into the first solvation layer of Na<sup>+</sup> in BPG, which significantly participates in interphase formation. According to the P–O and B–O radical distribution functions from MD simulations, the peak of B–O in BPG clearly appears at a shorter distance than that of P–O in PG (Supplementary Fig. 14), suggesting a preferential combination between B and O species.

To confirm the above calculations, XPS (P 2s/B 1s spectra) depth profiling results (Supplementary Figs. 15 and 16) with different sputtering time show that the outermost layer of SEI in PG has P–O–F and P–F species but there is a strong signal related to the B–O species in BPG. Although similar organic–inorganic hybrid SEI structures are formed in PG and BPG, the SEI of BPG is obviously thinner than that of PG from the rapid growth of the Na signal during sputtering. Concerning inner layers, few P–O species are present in PG while B–O species are still rich in BPG. Fourier transform infrared spectroscopy (FTIR) results (Supplementary Fig. 17) identify the existence of B–O species as well.

Further investigations about the three-dimensional distribution of passivation products are based on time-of-flight secondary-ion mass spectrometry (ToF-SIMS) analyses with deeper detection in Fig. 3c. It was surprisingly found that the SEI of B-containing species present a two-dimensional distribution along the z axis, while

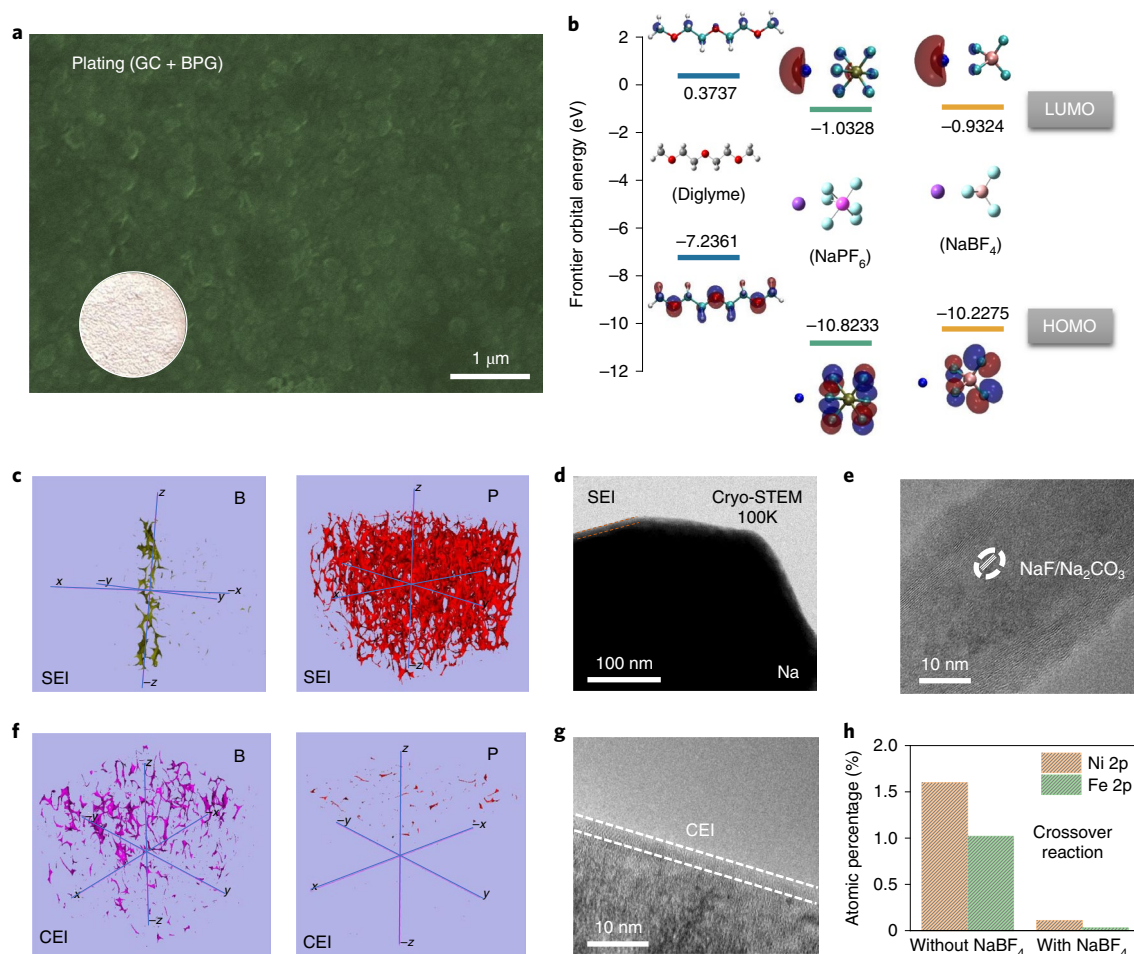


**Fig. 3 | Selection and assessment of electrolytes and SEI/CEI films.** **a**, SEM images of Na deposition in the AFNBs using GC and BPG after ten cycles. The inset shows the related digital image. **b**, Molecular orbital energies of  $\text{NaPF}_6$ ,  $\text{NaBF}_4$  and diglyme, including lowest unoccupied molecular orbital (LUMO) energies and highest occupied molecular orbital (HOMO) energies. Colours for different atoms: white for H, purple for Na, grey for C, red for O, lilac for P, green for F and pink for B. Colours for electron density contours: deep red for positive and blue for negative. **c**, TOF-SIMS three-dimensional views of the SEI film of Na in BPG; the two three-dimensional views are for  $\text{B}^+$  and  $\text{P}^-$  secondary ions. **d**, Annular bright field cryo-STEM image of Na in BPG after ten cycles. **e**, High-resolution TEM images of SEI film on GC after Na stripping (ten cycles). The circle in the middle indicates formation of a few nanocrystals. **f**, TOF-SIMS three-dimensional views of the CEI film of the cathode in BPG after ten cycles. Different distributions of  $\text{B}^+$  and  $\text{P}^-$  secondary ions are shown. **g**, High-resolution TEM image of cathode and CEI film in BPG after ten cycles. The white dashed line denotes the thin CEI film. **h**, The amount of transition metal (Fe and Ni) deposited on the cycled Na anode in PG and BPG (ten cycles) from XPS results (Fe 2p and Ni 2p).

P-containing species demonstrate a dense and three-dimensional distribution in BPG. It was believed that these sheet-like B–O species play a role in repairing the cracks along the  $x$ – $y$  axis, as depicted in Fig. 1. The thin SEI with a thickness of  $\sim 10$  nm (Fig. 3d) on deposited Na in BPG was investigated via cryogenic scanning transmission electron microscopy (cryo-STEM) at 100 K. Energy-dispersive X-ray spectrometer results (Supplementary Fig. 18) show that the B element signal is weaker than that of P element, indicating a small B ratio in SEI. High-resolution cryo-STEM images (Fig. 3e and Supplementary Fig. 19) show amorphous SEI structure with little NaF or  $\text{Na}_2\text{CO}_3$  nanocrystals. Actually, the inorganic B–O species, usually as a component of glass, tend to have a poor crystallinity with potential uniform ion flux and favourable flexibility.

As for the CEI on the cathode surface, XPS analyses (Supplementary Figs. 20 and 21) show that B–O and B–O–F species appear with  $\text{NaBF}_4$  addition. Moreover, ToF-SIMS results (Fig. 3f) of CEI in BPG show that B-containing species present a three-dimensional distribution along the  $z$  axis in the inner layer of CEI but there are few P-containing species in the outer layer of CEI. Thus, CEI is obviously different from the SEI as depicted in

Fig. 1, which is induced by the different reaction sequence of  $\text{NaBF}_4$  on the cathode and anode side. A high-resolution TEM image (Fig. 3g) of the cathode in BPG demonstrates a uniform and amorphous CEI film with the thickness of  $\sim 3$  nm. Even though CEI is very thin, it can affect SEI and even Na deposition via a crossover reaction of transition metal ions. As demonstrated by XPS analysis of the SEI, the dissolution of Ni and Fe species are significantly suppressed after introduction of  $\text{NaBF}_4$  (Fig. 3h). Thus, the cathode side tends to produce a thin and robust passivation layer on its surface in BPG<sup>33</sup>, which can effectively protect the structural integrity of cathode materials and prevent the side reactions with the electrolyte.

### Cooperative interfaces inhibit dead Na formation

To determine the origin of the highly reversible Na deposition and the roles of the built cooperative interfaces, we carried out several in situ and ex situ tests for the AFNBs with different current collectors and electrolytes. The Na plating processes were first recorded via in situ optical microscopic analysis in the coin-type AFNBs with open configuration. For the AFNB with AC and PG, lump-like Na deposition initially occurs at a certain position and rapidly spreads

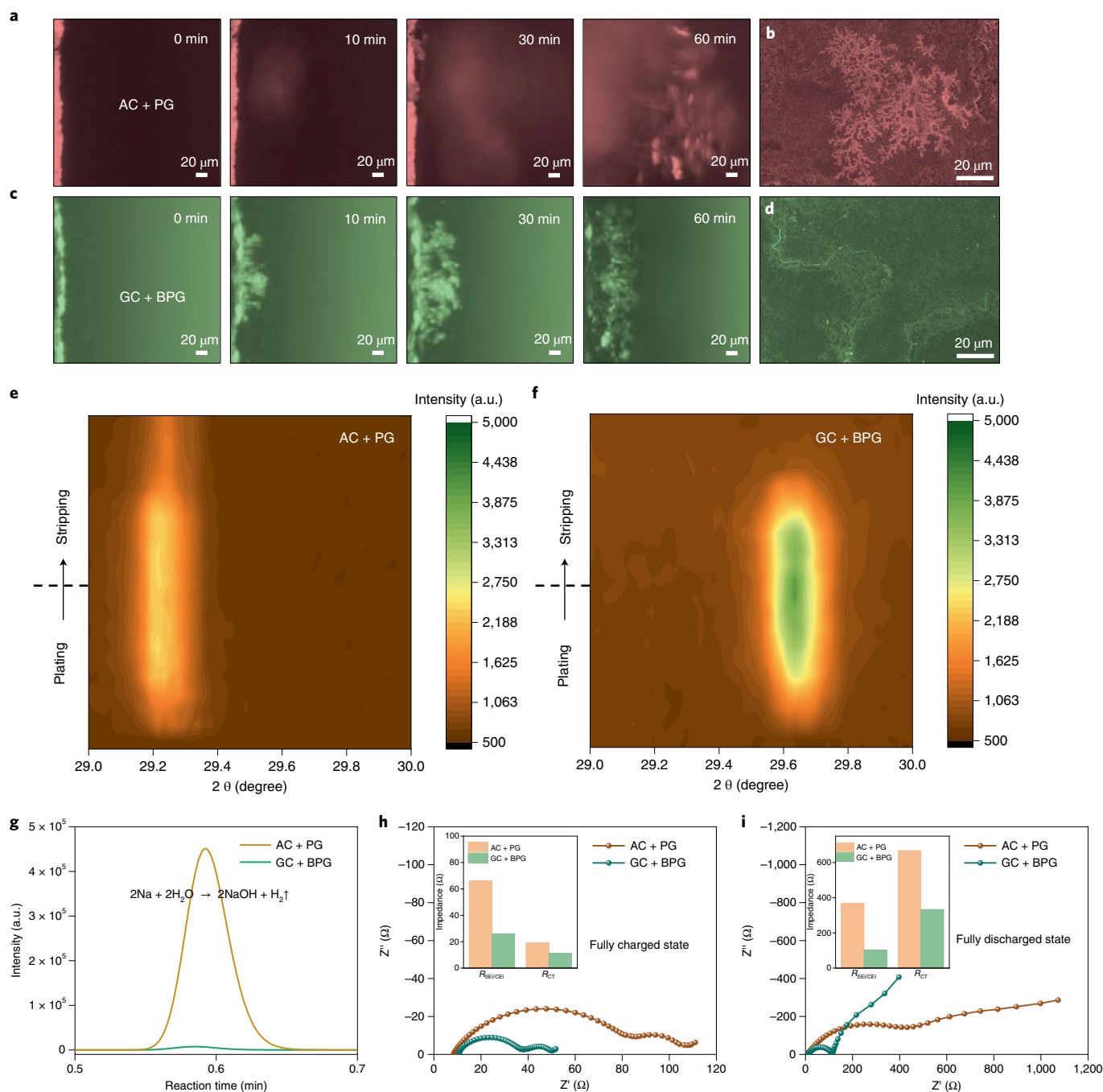


**Fig. 4 | Performance and mechanism of cooperative interfaces.** **a,c**, In situ optical microscopic observation of Na plating in the AFNBs using AC plus PG (**a**) and GC plus BPG (**c**). **b,d**, SEM images of Na deposition in the coin-type AFNBs using AC plus PG (**b**) and GC plus BPG (**d**) and after 20 cycles. **e,f**, In situ X-ray diffraction patterns collected during the first cycling process of the AFNBs using AC plus PG (**e**) and GC plus BPG (**f**). The dotted lines are used to distinguish charging and discharging. **g**, Titration gas chromatography chromatogram of gases with  $\text{H}_2$  after  $\text{H}_2\text{O}$  titration on the Na anode from AFNBs. **h,i**, Ex situ electrochemical impedance spectra curves of the AFNBs in a fully charged state (**h**) and fully discharged state (**i**). The inset shows related dependence of  $R_{\text{SEI/CEI}}$  and  $R_{\text{CT}}$ .

along a three-dimensional direction (Fig. 4a). The huge volume expansion induces non-uniformity and fracture of SEI, disturbing the distribution of local current density on the Na surface, thus, the uneven Na plating generates Na dendrites with a bush-like structure (Fig. 4b). Instead, for the AFNB with GC and BPG, Na gradually spreads out across GC surface via a two-dimensional deposition (Fig. 4c), resulting in flat and densely packed Na domains (Fig. 4d). Atomic force microscopy further confirms the smaller

roughness of Na formed in GC and BPG (Supplementary Fig. 22), and its SEI has larger elasticity (nano-mechanical property analyses in Supplementary Fig. 23).<sup>†</sup>

In Fig. 4e,f, in situ X-ray diffraction (XRD) was measured to detect the structural evolution of Na in sealed-type AFNBs. During the charging process, the emerging peaks located at about  $29^\circ$  in both systems were assigned to the (110) plane of Na metal. However, the peak intensity of the maximum Na deposition using AC and PG

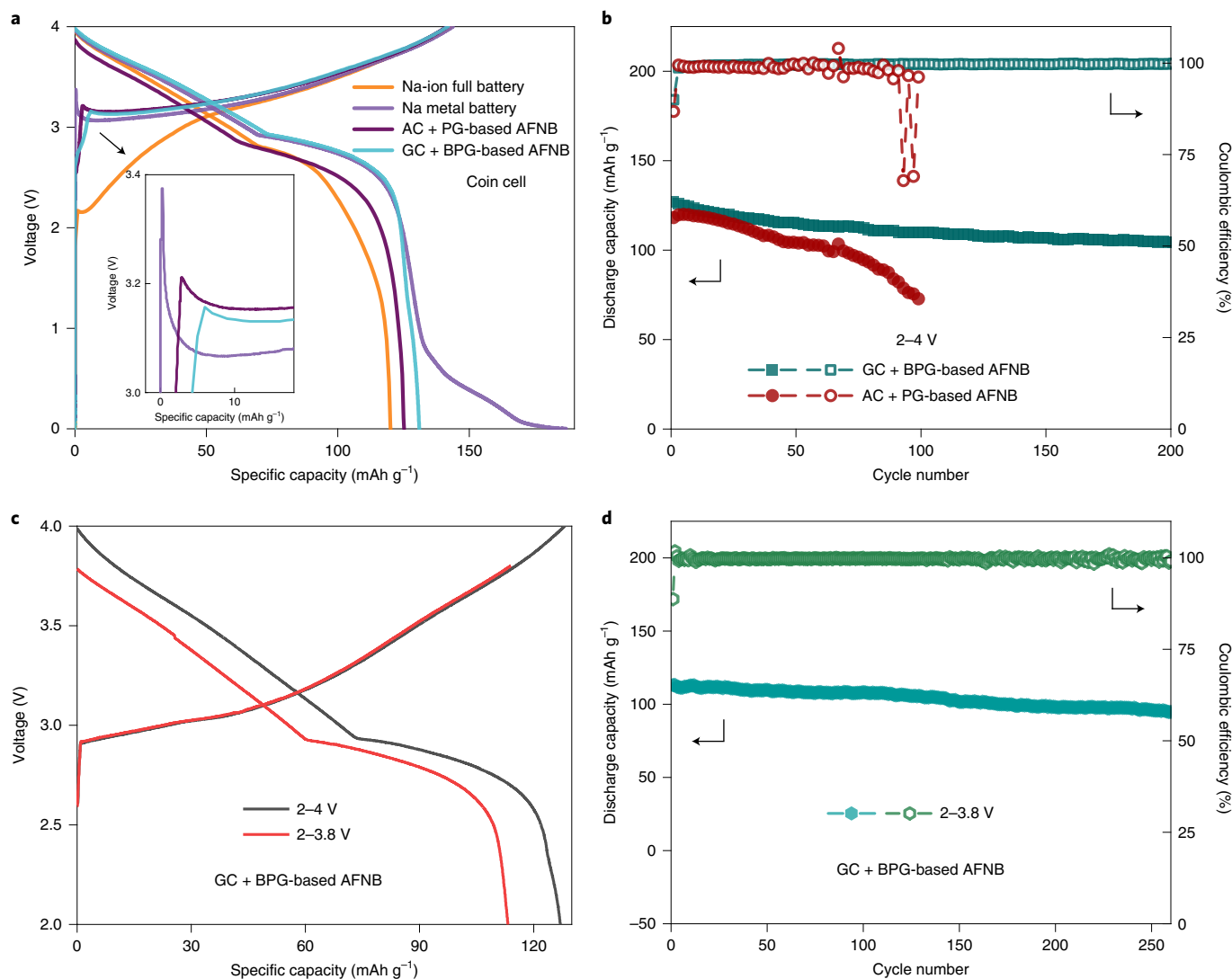


**Fig. 5 | Comparison among different kinds of Na-based batteries.** **a**, Galvanostatic initial discharge/charge curves of different kinds of Na-based batteries (coin cells) between 0 V and 4 V at a current rate of 0.5 C ( $1\text{C} = 127\text{ mAh g}^{-1}$ ). The inset shows the enlarged curves. **b**, Cyclic capability of AFNBs between 2 V and 4 V at a current rate of 0.5 C. **c**, Galvanostatic third discharge/charge curves of the AFNBs using GC plus BPG with different cut-off voltages. **d**, Cyclic capability of the AFNB using GC and BPG between 2 V and 3.8 V at a current rate of 0.5 C.

is weaker, probably indicating a crystallinity difference between the two systems. More importantly, there is a residual Na signal using AC and PG at the end of discharging process, but the Na (110) peak completely disappears using GC and BPG, illustrating the highly reversible Na plating and stripping. The sectional SEM images further show that the deposited Na from the AFNB using AC and PG has a higher porosity and larger thickness in Supplementary Fig. 24, suggesting more inactive Na ('dead Na') are generated during cycling. To quantitatively determine the 'dead Na' in these two systems,  $\text{H}_2\text{O}$  titration with gas chromatography was performed, where the GC and BPG system has obviously less  $\text{H}_2$  escape (Fig. 4g), indicating little 'dead Na' was generated during cycling<sup>34</sup>. The electrochemical impedance spectra (EIS) of the AFNBs are shown in Fig. 4h,i. The high-frequency semicircle represents the charge transfer impedance ( $R_{ct}$ ), and the semicircle in low frequency corresponds with the interface impedance about SEI and CEI films ( $R_{SEI/CEI}$ ). An equivalent circuit diagram for EIS plots is shown in Supplementary Fig. 25. Regardless of charged or discharged state, the resistances of charge transfer and  $\text{Na}^+$  diffusion across the interfaces are much lower using GC and BPG. Therefore, the results further proved that

the cooperative interfaces induced by GC and BPG are able to suppress dead Na formation and facilitate  $\text{Na}^+$  diffusion, benefiting the uniform plating and reversible stripping of Na during cycling, as shown in Fig. 1.

### Electrochemical performances and safety assessment

To evaluate the effect of cooperative interfaces in more realistic conditions, AFNBs ( $\text{AC}||\text{Na}[\text{Cu}_{1/9}\text{Ni}_{2/9}\text{Fe}_{1/3}\text{Mn}_{1/3}]\text{O}_2$  and  $\text{GC}||\text{Na}[\text{Cu}_{1/9}\text{Ni}_{2/9}\text{Fe}_{1/3}\text{Mn}_{1/3}]\text{O}_2$ ) were assembled, and corresponding electrochemical performances were measured. A NIB based on a carbon anode ( $\text{C}||\text{Na}[\text{Cu}_{1/9}\text{Ni}_{2/9}\text{Fe}_{1/3}\text{Mn}_{1/3}]\text{O}_2$ ) and a NMB ( $\text{Na}||\text{Na}[\text{Cu}_{1/9}\text{Ni}_{2/9}\text{Fe}_{1/3}\text{Mn}_{1/3}]\text{O}_2$ ) are also prepared to make a comparison.

In their initial charge process, the nucleation preferentially occurs with the characteristics of the sharp peaks in Fig. 5a. The nucleation overpotential increases in the order of GC + BPG-based AFNB < AC + PG-based AFNB < NMB, indicating the modification of electrolytes and current collectors enables a favourable nucleation. In the discharge process, the discharge capacity increases in the order of NIB ( $120\text{ mAh g}^{-1}$ ) < AC + PG-based AFNB ( $125\text{ mAh g}^{-1}$ ) < GC + BPG-based AFNB ( $130\text{ mAh g}^{-1}$ ) < NMB

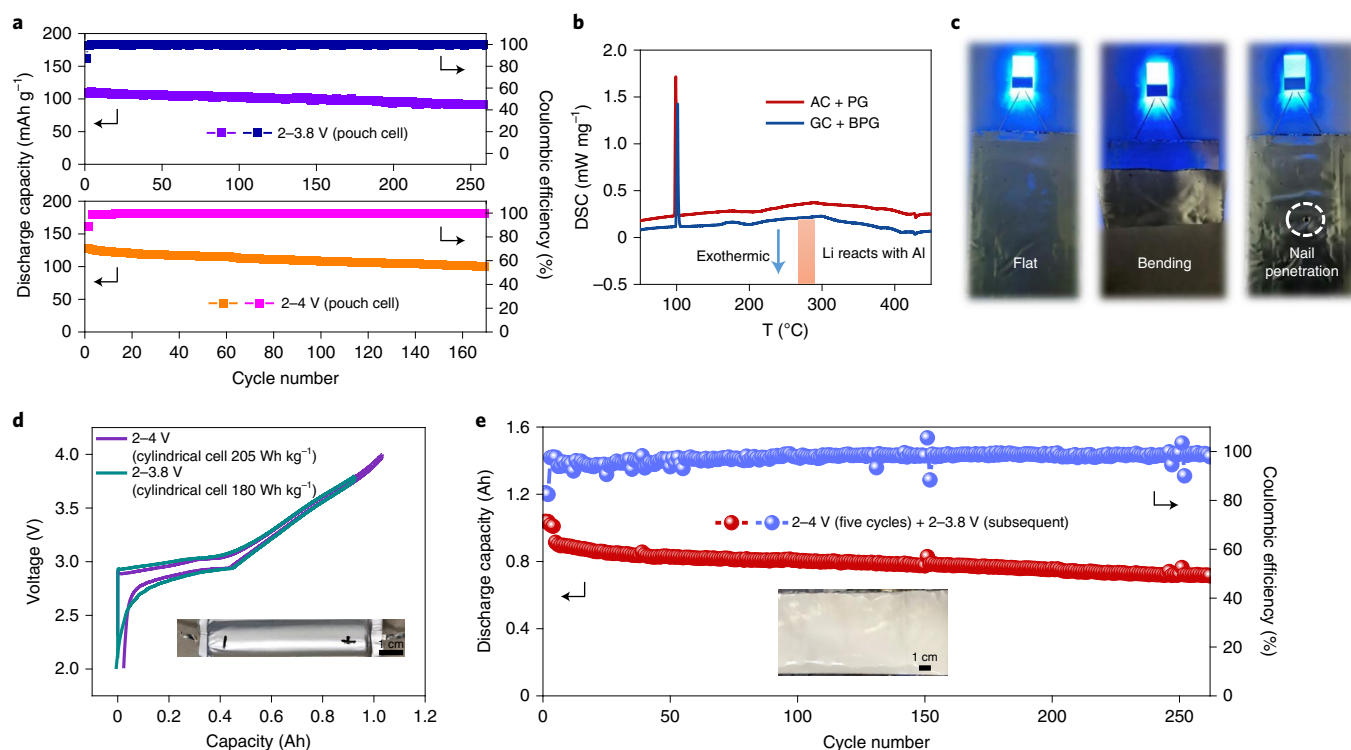


**Fig. 6 | Electrochemical performances and safety assessment of proposed Na batteries with cooperative interfaces.** **a**, Cyclic capability of the AFNBs (single-layer pouch cell) using GC and BPG with different cut-off voltages at a current rate of 0.5 C. **b**, DSC curves of the deposited Na, including current collectors from the 30 mAh level single-layer AFNBs (the orange bar is the DSC exothermic peak at the Li-Al reaction). **c**, The AFNB (single-layer pouch cell) using GC and BPG with fully charged state lighting a bulb after bending deformation and further nail penetration. **d**, Galvanostatic third discharge/charge curves of the AFNBs (cylindrical cell) using GC plus BPG with different cut-off voltages at a current rate of 0.5 A. The inset shows a picture of the 1 Ah level anode-free cylindrical cell with  $>200 \text{ Wh kg}^{-1}$  energy density. **e**, Cyclic capability of the AFNB (cylindrical cell) using GC and BPG at a current rate of 0.5 A. The inset shows a picture of the deposited Na anode collected from the AFNB (cylindrical cell) using GC and BPG. The areal capacity of coin cells or pouch cells is  $\sim 2 \text{ mAh cm}^{-2}$  while that of cylindrical cells is  $\sim 3 \text{ mAh cm}^{-2}$ .

( $186 \text{ mAh g}^{-1}$ ). The abnormal discharge capacity of NMB originates from the electrolyte reduction to form copious CEI and/or extra electrolyte decomposition, which suffers a rapid decay (Supplementary Figs. 26–28). Thus, the AFNBs without an extra Na source are similar to NIBs, which can be discharged to 0 V to facilitate safe transportation and large-scale battery management. Moreover, the initial Coulombic efficiency and average discharge voltage of GC+BPG-based AFNB ( $\sim 92\%$ ; 3.05 V) are higher than that of AC+PG-based AFNB ( $\sim 88\%$ ; 2.85 V) and NIB ( $\sim 83\%$ ; 2.96 V). In Fig. 5b, the cycling tests of two AFNBs were also performed, and the capacity retention of GC+BPG-based AFNB is 82% after 200 cycles but that of AC+PG-based AFNB is only 61% after 100 cycles with unstable CEs. Considering the low oxidative resistance of the ether electrolyte, the cycling lifetime of AFNBs can be further extended to over 260 cycles (capacity retention: 84%) through selecting a reasonable upper cut-off voltage of 3.8 V (only 11% capacity loss in Fig. 5c) in Fig. 5d.

Furthermore, we assembled 30 mAh single-layer pouch cells based on GC and BPG. It can be seen that their cycling stabilities are similar to that of coin cells in Fig. 6a, indicating that increasing the amount of deposited Na will not reduce the performance of AFNB. The thermal feature of fully charged AFNB pouch cells are further evaluated by a differential scanning calorimeter (DSC). It is found that deposited Na metals in both AFNBs display endothermic peaks only where the GC+BPG-based AFNB has a higher initial endothermic temperature ( $101.3^\circ\text{C}$  versus  $97.7^\circ\text{C}$  of pure Na metal) in Fig. 6b, suggesting the smooth morphology of deposited Na induced by cooperative interfaces can enhance the thermal

stability of AFNB<sup>14,35</sup>. More importantly, compared with the Li-based anode-free batteries, Na will not react with Al to produce an exothermic peak (but internal shortage may occur if melted Na diffuses into the cathode side at high temperature<sup>3</sup>). Besides, AFNB pouch cells are able to pass through abusive tests, including bending deformation and nail penetration, delivering a stable current to light up the blue light-emitting diode without fire in Fig. 6c.

To further explore the practical application of AFNBs, an Ah-level anode-free cylindrical cell based on GC and BPG (lean electrolyte) was fabricated. Very high energy densities (calculated based on all cell components) of  $180 \text{ Wh kg}^{-1}$  (0.91 Ah) in the voltage range of 2–3.8 V and  $205 \text{ Wh kg}^{-1}$  (1.03 Ah) in 2–4 V were obtained (Fig. 6d), which rivals the energy density of a typical LFP/graphite LIB. Besides, it can support very stable long cycling (capacity retention: 80% in 2–3.8 V after 260 cycles) at a moderate rate (0.5 A) in Fig. 6e. From the inset, a deposited Na anode collected from the cylindrical cell after 30 cycles shows a smooth and shiny surface, relating to the high average CE. Furthermore, the in situ deposited Na foil can even act as the fresh ultra-thin Na anode (metallic Na extraction technology) in other NMBs.

## Conclusions

In summary, AFNBs with cooperative interfaces were fabricated through interfacial engineering strategy by adopting a BPG electrolyte, GC current collector and layered oxide cathode. Smooth Na deposition was achieved based on the small and uniform Na nucleation on GC. Robust SEI and CEI were also built. It is revealed from advanced characterization techniques and MD simulations that due

to the special solvation configuration of BPG, B–O species present a two-dimensional distribution in the outer layer of SEI but a three-dimensional distribution in the inner layer of CEI. This effectively suppresses the formation of dead Na or Na dendrite, repairs formed cracks during Na plating and stripping, protects the structural integrity of the cathode and prevents side reactions with the electrolyte. The assembled Ah-level AFNBs with high safety deliver an energy density over 200 Wh kg<sup>-1</sup>, which is very cost effective given the employment of the Co, V-free layered oxide cathode, the lean non-concentrated electrolyte, the thin-coating current collector and the dry room production. Moreover, benefitting from the built cooperative interphases, the cycle life of AFNBs is prolonged to be over 260 cycles without extra stack pressure or high operation temperature. The current bottlenecks of AFNBs are low energy density and limited cycling stability under practical conditions. In this regard, by demonstrating a high-voltage region application with a lean ether electrolyte, this work provides a prototype cell solution towards high-performance Na batteries. Our ideas of rational interface design are expected to stimulate further optimization of cell components, facilitating large-scale utilization of AFNBs in the future.

## Methods

**Materials preparation.** The AC- and GC-coated Al is prepared by the coating machine. Firstly, the carbon black (BLUEGLOWNANO) and carbon fibre (The First Element Nanotech) are dispersed into 1-Methyl-2-pyrrolidone (NMP) using polyvinylpyrrolidone (PVP) and polyvinylidene fluoride (PVDF) as binders (mass ratio of carbon:PVP:PVDF:NMP = 4:1:1:94). Then, the extrusion-coating technology on Al foil is implemented followed by baking and rolling processes. During the coating process, the baking temperature is at ambient temperature (~25 °C). The rolling pressure is 5–10 ton. The final mass loadings of both AC and GC coatings are ~0.4 mg cm<sup>-2</sup> but the thickness of the AC coating (~4 μm) is lower than that of the GC coating (~8 μm) and the porosity of the AC coating (~47%) is lower than that of the GC coating (~78%).

The layered O3-type Na[Cu<sub>1/9</sub>Ni<sub>2/9</sub>Fe<sub>1/3</sub>Mn<sub>1/3</sub>]O<sub>2</sub> cathode materials were synthesized by high-temperature calcination according to the early report<sup>36</sup>. The composition of the cathode (total mass loading: ~16 mg cm<sup>-2</sup>) slurry was 94.5 wt% active materials, 2.5 wt% Super P and 3 wt% PVDF. The mass loading of only active cathode materials is ~15 mg cm<sup>-2</sup>. The electrode slurries were casted on Al foil followed by a drying process under vacuum. The electrolytes, including PG and BPG, used for the cells are *x* M (mol l<sup>-1</sup>) NaPF<sub>6</sub> (Kishida Chemical, 99%) or NaBF<sub>4</sub> (ALADDIN, 99.9% metals basis) dissolved in diglyme (Sigma-Aldrich, 99.5%) without any functional additives. All the electrolytes were prepared and dried using molecular sieves (4 Å) in a glove box under high-purity argon gas.

**Electrochemical measurements.** Coin cells (CR2032) were assembled in an argon-filled glove box. The amount of electrolyte used for a coin cell is 50 μl. Glass fibre (Whatman GF/A) plus Celgard 3501 membrane was utilized as the separator. The matched anode in Na-ion full cell and Na metal half cell using PG as an electrolyte is disordered carbon materials (HiNa, P/N ratio for the Na-ion full cell is 1:1.05, and the loading mass is ~6.5 mg cm<sup>-2</sup>) and Na metal (Alfa), respectively. The current collectors were used in AFNBs. The single-layer pouch cells and 13,650-type cylindrical cell were assembled in a dry room using Na[Cu<sub>1/9</sub>Ni<sub>2/9</sub>Fe<sub>1/3</sub>Mn<sub>1/3</sub>]O<sub>2</sub> as the cathode and AC or GC foil as the anode, Celgard 3501 membrane as the separator, PG or BPG as electrolyte (2 g Ah<sup>-1</sup>) and Al-plastic film as packaging. The operation temperature of the cells for in situ optical and XRD tests is ambient temperature (~25 °C) but that of other cells is 25 °C controlled by oven thermostats. The charge and discharge tests of full cells were performed on the Land battery test systems (CT3001A or CT2001A) or Neware battery test system (CT-4008). LSV measurements and Tafel plots were obtained on a CHI 600E electrochemical workstation (0.1 mV s<sup>-1</sup>). LSV measurements were obtained from the Na|stainless steel cells using a PG or BPG electrolyte between the open circuit voltage of these cells (~2.7 V) and 6.5 V at a scan rate of 0.1 mV s<sup>-1</sup>. Tafel plots were obtained from the symmetric Na|Na cells using a PG or BPG electrolyte between -0.2 V and 0.2 V at a scan rate of 0.1 mV s<sup>-1</sup>. EIS was recorded in a frequency range from 10 mHz to 10<sup>5</sup> kHz (IM6e Zahner electrochemical workstation). Ex situ EIS curves of the AFNBs (cell type: coin cell) with fully charged state and fully discharged state, which correspond to the 1st cycle between 0 V and 4 V at a current rate of 0.5 C (1 C = 127 mAh g<sup>-1</sup>) at 25 °C.

**Characterizations.** The morphologies of the samples were investigated by SEM (Hitachi-S4800) and TEM (FEI Tecnai G2 F20). All cryo-TEM characterizations were carried out using a JEOL JEM-F200 microscope with a cryo transfer holder (Fischione, model 2550) under cryogenic temperatures (100 K) at 200 kV. The structures of the samples were investigated by Raman spectra using a LabRAM JY-HR 800 spectrometer with a 532 nm laser. The electronic conductivity values

were obtained from a four-point-probe conductivity metre (MCP-PD51). An automatic contact angle measuring instrument (DSA30S) was used to test the wettability. The surface chemical state was determined by XPS using a PHI 5000 VersaProbe III instrument (Scanning ESCA Microprobe) with Al Kα X-ray source, 15 kV X-ray beam (analysis area: 200 μm × 200 μm) and Ar<sup>+</sup> etching (sputtering rate: 3.9 nm min<sup>-1</sup> for SiO<sub>2</sub>). All spectra were calibrated with the C1s photoemission peak at 284.8 eV to correct for the charging effect. FTIR was performed by a Bruker VERTEX 80 V spectrophotometer in attenuated total reflection mode (not transmission mode) in a glove box. TOF-SIMS analysis was conducted with a PHI nanoTOF II spectrometer with a 30 keV Bi<sub>3</sub><sup>+</sup> acquisition ion beam and a 1 kV Ar<sup>+</sup> sputtering ion beam for electrodes, respectively. During depth profiling, the typical acquisition area was 100 μm × 100 μm (positive mode) or 60 μm × 60 μm (negative mode) and centred within the Ar<sup>+</sup> 500 μm × 500 μm sputtered area (sputtering rate: 3 nm min<sup>-1</sup> for SiO<sub>2</sub>). To determine the amount of 'dead Na', 0.5 ml of H<sub>2</sub>O was injected into the container to react with a stripped sample completely for 2 h, when no bubbles were visible. The H<sub>2</sub> concentration was measured by a Shimadzu Nexis GC-2030 system equipped with a barrier ionization discharge detector. A gas-tight syringe was used to transfer 50 μl of the resultant gas from the container into the gas chromatography system. DSC were employed via a NETZSCH STA 449F3 thermal analyser from room temperature to 500 °C at a heating rate of 10 °C min<sup>-1</sup> under argon flow. For the ex situ measurements, the electrodes disassembled from the coin cells at different states of charge and discharge in an argon-filled glove box were washed in 1,2-Dimethoxyethane repeatedly followed by a drying processing in an argon-filled transferred tube (or air-free setup). In situ optical microscopic observation was carried out in a glove box at ambient temperature in a dark field, using metallographic microscope (LEICA, DM6) with a charge coupled device (CCD) camera in combine with a Land 2001A battery testing system (charging to 4 V at a current rate of 1 C at ambient temperature), as shown in Supplementary Fig. 29. In situ XRD measurements were carried out on a Bruker D8 Advance diffractometer equipped with a Cu Kα radiation (λ = 1.54 Å) in combination with a Land 2001A battery testing system. A specially designed Swagelok cell equipped with an X-ray-transparent aluminium window was used for the in situ measurements, as shown in Supplementary Fig. 30. The in situ XRD patterns were collected with an interval of 30 min on charge and discharge at a current rate of 0.1 C between 0–4 V at ambient temperature.

**Calculations.** The molecular orbital energies of NaPF<sub>6</sub>, NaBF<sub>4</sub> and diglyme were calculated using Gaussian 09 package towards NaPF<sub>6</sub>, NaBF<sub>4</sub> and diglyme. The density functional theory of B3LYP and a basis set of 6–31 G(d) was employed to optimize the geometry structure of molecules and a basis set of 6–311 + G (d, p) was used to calculate the single point energy based on the polarizable continuum model. For the LUMO and HOMO calculations of NaPF<sub>6</sub> and NaBF<sub>4</sub>, the solvent environment of diglyme was considered. The influence from the dielectric effect of diglyme (dielectric constant: 7.4) was investigated through the solvation model based on density.

For MD calculations, two electrolyte models were constructed to model the PG and BPG electrolytes. The PG electrolyte model contains 60 PF<sub>6</sub><sup>-</sup>, 60 Na<sup>+</sup> and 423 diglyme molecules. The BPG electrolyte model contains 54 PF<sub>6</sub><sup>-</sup>, 60 Na<sup>+</sup>, 6 BF<sub>4</sub><sup>-</sup> and 423 diglyme molecules. The molecular dynamics simulations were conducted in the Forcite module in Materials Studio of Accelrys Inc. A condensed-phase optimized molecular potentials for atomistic simulation studies (COMPASS II) force field was chosen for all the molecular dynamics simulations. Besides, the time step was fixed to be 1 fs. The electrolyte systems were equilibrated in the isothermal–isobaric ensemble (constant-pressure and constant-temperature, NPT) using the Berendsen barostat to maintain the pressure of 0.1 GPa with a decay constant of 0.1 ps for 2 ns. The temperature was set to be 298 K with a velocity scale thermostat. Then, the production runs of 8 ns were obtained in the canonical ensemble (constant-volume and constant-temperature, NVT) at 298 K. The simulation time was long enough to ensure reaching the equilibrium states of the electrolyte systems. Besides, the time step was fixed to be 1.5 fs to reduce waiting time.

## Data availability

The data supporting the findings of this study are available within the article and its Supplementary Information files.

Received: 26 October 2021; Accepted: 20 April 2022;

Published online: 2 June 2022

## References

- Vaalma, C., Buchholz, D., Weil, M. & Passerini, S. A cost and resource analysis of sodium-ion batteries. *Nat. Rev. Mater.* **3**, 18013 (2018).
- Usiskin, R. et al. Fundamentals, status and promise of sodium-based batteries. *Nat. Rev. Mater.* **6**, 1020–1035 (2021).
- Lee, B., Paek, E., Mitlin, D. & Lee, S. W. Sodium metal anodes: emerging solutions to dendrite growth. *Chem. Rev.* **119**, 5416–5460 (2019).
- Wang, Y. et al. Developments and perspectives on emerging high-energy-density sodium-metal batteries. *Chem* **5**, 2547–2570 (2019).

5. Zhao, C. et al. Solid-state sodium batteries. *Adv. Energy Mater.* **8**, 1703012 (2018).
6. Qian, J. et al. Anode-free rechargeable lithium metal batteries. *Adv. Funct. Mater.* **26**, 7094–7102 (2016).
7. Cahn, A. P., Muralidharan, N., Carter, R., Share, K. & Pint, C. L. Anode-free sodium battery through in situ plating of sodium metal. *Nano Lett.* **17**, 1296–1301 (2017).
8. Zhao, C. et al. Advanced Na metal anodes. *J. Energy Chem.* **27**, 1584–1596 (2018).
9. Wang, H., Matios, E., Luo, J. & Li, W. Combining theories and experiments to understand the sodium nucleation behavior towards safe sodium metal batteries. *Chem. Soc. Rev.* **49**, 3783–3805 (2020).
10. Mogensen, R., Brandell, D. & Younesi, R. Solubility of the solid electrolyte interphase (SEI) in sodium ion batteries. *ACS Energy Lett.* **1**, 1173–1178 (2016).
11. Iermakova, D. I., Dugas, R., Palacín, M. R. & Ponrouch, A. On the comparative stability of Li and Na metal anode interfaces in conventional alkyl carbonate electrolytes. *J. Electrochem. Soc.* **162**, A7060–A7066 (2015).
12. Nanda, S., Gupta, A. & Manthiram, A. Anode-free full cells: a pathway to high-energy density lithium-metal batteries. *Adv. Energy Mater.* **11**, 2000804 (2021).
13. Weber, R. et al. Long cycle life and dendrite-free lithium morphology in anode-free lithium pouch cells enabled by a dual-salt liquid electrolyte. *Nat. Energy* **4**, 683–689 (2019).
14. Louli, A. J. et al. Diagnosing and correcting anode-free cell failure via electrolyte and morphological analysis. *Nat. Energy* **5**, 693–702 (2020).
15. Qiao, Y. et al. A high-energy-density and long-life initial-anode-free lithium battery enabled by a  $\text{Li}_2\text{O}$  sacrificial agent. *Nat. Energy* **6**, 653–662 (2021).
16. Cohn, A. P. et al. Rethinking sodium-ion anodes as nucleation layers for anode-free batteries. *J. Mater. Chem. A* **6**, 23875–23884 (2018).
17. Rudola, A., Gajjala, S. R. & Balaya, P. High energy density in-situ sodium plated battery with current collector foil as anode. *Electrochem. Commun.* **86**, 157–160 (2018).
18. Lee, M. E. et al. Anode-free sodium metal batteries based on nanohybrid core-shell templates. *Small* **15**, 1901274 (2019).
19. Wang, H. et al. 3D  $\text{Ag@C}$  cloth for stable anode free sodium metal batteries. *Small Methods* **5**, e2001050 (2021).
20. Seh, Z. W., Sun, J., Sun, Y. & Cui, Y. A highly reversible room-temperature sodium metal anode. *ACS Cent. Sci.* **1**, 449–455 (2015).
21. Zhang, J. et al. Ethers illumine sodium-based battery chemistry: uniqueness, surprise, and challenges. *Adv. Energy Mater.* **8**, 1801361 (2018).
22. Lin, Z., Xia, Q., Wang, W., Li, W. & Chou, S. Recent research progresses in ether- and ester-based electrolytes for sodium-ion batteries. *InfoMat* **1**, 376–389 (2019).
23. Goktas, M. et al. Stable and unstable diglyme-based electrolytes for batteries with sodium or graphite as electrode. *ACS Appl. Mater. Interfaces* **11**, 32844–32855 (2019).
24. Zhou, L. et al. Engineering sodium-ion solvation structure to stabilize sodium anodes: universal strategy for fast-charging and safer sodium-ion batteries. *Nano Lett.* **20**, 3247–3254 (2020).
25. Mazzali, F. et al. Designing a high-power sodium-ion battery by in situ metal plating. *ACS Appl. Energy Mater.* **2**, 344–353 (2018).
26. Li, W.-J. et al. Commercial prospects of existing cathode materials for sodium ion storage. *Adv. Energy Mater.* **7**, 1700274 (2017).
27. Liu, S. et al. Porous Al current collector for dendrite-free Na metal anodes. *Nano Lett.* **17**, 5862–5868 (2017).
28. Li, Y., Lu, Y., Adelhelm, P., Titirici, M. –M. & Hu, Y.-S. Intercalation chemistry of graphite: alkali metal ions and beyond. *Chem. Soc. Rev.* **48**, 4655–4687 (2019).
29. Zhang, X. et al. Dendrite-free and long-cycling sodium metal batteries enabled by sodium-ether cointercalated graphite anode. *Adv. Funct. Mater.* **31**, 2009778 (2021).
30. Wang, S. et al. Stable sodium metal batteries via manipulation of electrolyte solvation structure. *Small Methods* **4**, 1900856 (2020).
31. Le, P. M. L. et al. Excellent cycling stability of sodium anode enabled by a stable solid electrolyte interphase formed in ether-based electrolytes. *Adv. Funct. Mater.* **30**, 2001151 (2020).
32. Wang, J. et al. Fire-extinguishing organic electrolytes for safe batteries. *Nat. Energy* **3**, 22–29 (2018).
33. Yang, L. et al. Harnessing the surface structure to enable high-performance cathode materials for lithium-ion batteries. *Chem. Soc. Rev.* **49**, 4667–4680 (2020).
34. Fang, C. et al. Quantifying inactive lithium in lithium metal batteries. *Nature* **572**, 511–515 (2019).
35. Fu, L. et al. A lithium metal anode surviving battery cycling above 200 °C. *Adv. Mater.* **32**, 2000952 (2020).
36. Mu, L. et al. Electrochemical properties of novel  $\text{O}_3\text{-NaCu}_{1/9}\text{Ni}_{2/9}\text{Fe}_{1/3}\text{Mn}_{1/3}\text{O}_2$  as cathode material for sodium-ion batteries. *Energy Storage Sci. Technol.* **5**, 324–328 (2016).

## Acknowledgements

This work was supported by the National Natural Science Foundation (NSFC) of China (51725206, 52122214 and 52072403), the Strategic Priority Research Program of the Chinese Academy of Sciences (XDA21070500), the Youth Innovation Promotion Association of the Chinese Academy of Sciences (2020006) and Beijing Municipal Natural Science Foundation (2212022).

## Author contributions

Y.-S.H. conceived and designed this work; Yuqi L. prepared the materials and carried out the electrochemical measurements and calculations; Yuqi L., Q.Z. and Yu L. assembled the pouch cells and cylindrical cells. Yuqi L., S.W., F.D., J.L. and X.Z. carried out the ex situ or in situ characterizations and analysis; Yuqi L., Yaxiang L. and Y.-S.H. wrote the manuscript; all the authors participated in the discussion to improve the paper and made revisions of the whole manuscript.

## Competing interests

X.W. and H.L. are employed at Tianmu Lake Institute of Advanced Energy Storage Technologies. Q.Z., X.Q. and Y.-S.H. are employed at HiNa Battery Technology Co., Ltd.

## Additional information

**Supplementary information** The online version contains supplementary material available at <https://doi.org/10.1038/s41560-022-01033-6>.

**Correspondence and requests for materials** should be addressed to Yaxiang Lu or Yong-Sheng Hu.

**Peer review information** *Nature Energy* thanks Naoaki Yabuuchi and the other, anonymous, reviewer(s) for their contribution to the peer review of this work.

**Reprints and permissions information** is available at [www.nature.com/reprints](http://www.nature.com/reprints).

**Publisher's note** Springer Nature remains neutral with regard to jurisdictional claims in published maps and institutional affiliations.

© The Author(s), under exclusive licence to Springer Nature Limited 2022